Since January 2020 Elsevier has created a COVID-19 resource centre with free information in English and Mandarin on the novel coronavirus COVID-19. The COVID-19 resource centre is hosted on Elsevier Connect, the company's public news and information website.

Elsevier hereby grants permission to make all its COVID-19-related research that is available on the COVID-19 resource centre - including this research content - immediately available in PubMed Central and other publicly funded repositories, such as the WHO COVID database with rights for unrestricted research re-use and analyses in any form or by any means with acknowledgement of the original source. These permissions are granted for free by Elsevier for as long as the COVID-19 resource centre remains active.

Journal of Aerosol Science 171 (2023) 106166

Contents lists available at ScienceDirect

Journal of Aerosol Science

journal homepage: www.elsevier.com/locate/jaerosci

Fluid-structure interaction analysis of airflow, structural mechanics and aerosol dynamics in a four-generation acinar model

Penghui Li [a], Weiqi Guo [b], Jinbo Fan [a], Chen Su [a], Xiuguo Zhao [a], Xinxi Xu [a,*]

[a] Department of Medical Support Technology, Institute of Systems Engineering, Academy of Military Sciences, Tianjin, 300161, China
[b] Department of Building Science, Tsinghua University, Beijing, 100084, China

ARTICLE INFO

Handling Editor: Chris Hogan

Keywords:
FSI
Aerosol deposition
Structural mechanics
Pulmonary acinus
CFD

ABSTRACT

Elucidating the aerosol dynamics in the pulmonary acinar region is imperative for both health risk assessment and inhalation therapy, especially nowadays with the occurrence of the global COVID-19 pandemic. During respiration, the chest's outward elastic recoil and the lungs' inward elastic recoil lead to a change of transmural pressure, which drives the lungs to expand and contract to inhale and expel airflow and aerosol. In contrast to research using predefined wall motion, we developed a four-generation acinar model and applied an oscillatory pressure on the model outface to generate structure deformation and airflow. With such tools at hand, we performed a computational simulation that addressed both the airflow characteristic, structural mechanics, and aerosol dynamics in the human pulmonary acinar region. Our results showed that there is no recirculating flow in the sac. The structural displacement and stress were found to be positively related to the change of model volume and peaked at the end of inspiration. It was noteworthy that the stress distribution on the acinar wall was significantly heterogeneous, and obvious concentrations of stress were found at the junction of the alveoli and the ducts or the junction of the alveoli and alveoli in the sac. Our result demonstrated the effect of breathing cycles and aerosol diameter on deposition fraction and location of aerosols in the size range of 0.1–5 μm. Multiple respiratory cycles were found necessary for adequate deposition or escape of submicron particles while having a negligible influence on the transport of large particles, which were dominated by gravity. Our study can provide new insights into the further investigation of airflow, structural mechanics, and aerosol dynamics in the acinar depth.

1. Introduction

There are up to 400 million alveoli (Matthias et al., 2004) arranged in clusters throughout the lungs, moving oxygen and carbon dioxide (CO_2) into and out of the bloodstream. However, ambient pollutants and virus-laden aerosols can be inhaled into the pulmonary acinar region, posing a severe risk to human health (Kato et al., 2003; Nemmar et al., 2002; Singh et al., 2019; Sundh et al., 2015). Moreover, inhalation therapy is getting used widely with advantages such as its non-invasive nature and low side effects (Amirav & Newhouse, 2012; Ari & Fink, 2013; Sung et al., 2007; Wu et al., 2021), especially nowadays with the occurrence of global COVID-19 pandemic (Leung, 2021; Sznitman, 2022). Revealing the mechanisms of transport and deposition of inhaled particles in the

* Corresponding author.
E-mail address: xuxx@npec.org.cn (X. Xu).

https://doi.org/10.1016/j.jaerosci.2023.106166
Received 19 January 2023; Received in revised form 27 February 2023; Accepted 7 March 2023
Available online 13 March 2023
0021-8502/© 2023 Elsevier Ltd. All rights reserved.

lungs contributes to reducing the damage of toxic and harmful aerosols on human health and increasing the targeted deposition rate of drug particles for maximum therapeutic efficacy. Therefore, it is necessary to elucidate the transport and deposition of aerosols in the pulmonary acinar region for both health risk assessment and inhalation therapy.

The lungs are constantly expanding and contracting to inhale and expel airflow and aerosol during respiration, which is the primary driver of the motion of airflow and aerosol. Therefore, accurate lung movements are essential to obtain the flow field and aerosol motion characteristics in the acinar region. Over the past few decades, significant efforts have been taken to resolve and capture the motion of the acinus. One of the methods is to use a dynamic mesh approach to predefine the movement of the models so that they can follow a programmed pattern of expansion and contraction. And the movement is frequently set up as geometrically self-similar (i.e., isotropic) according to research (Ardila et al., 1974; Gil et al., 1979; Gil & Weibel, 1972). For example, Tsuda et al. (1995) developed a simplified two-dimensional alveolar model and investigated the effect of sinusoidal isotropic motion of the alveolar model on the flow field, which was found to be closely related to the ratio of alveolar flow and duct flow. Sznitman et al. (2007) simulated three-dimensional alveolar flows in an alveolated duct at each generation of the pulmonary acinar tree. They demonstrated that inherent wall motion is essential to understand natural acinar flow phenomena. Ma and Darquenne (2012) studied the effect of gravity and airway asymmetry on the dispersion of 1 μm particles in a single alveolar sac and four-generation (g4) bifurcating airways that deformed homogeneously during breathing. Their results concluded that aerosol dispersion was strongly correlated with model volume. Hofemeier et al. (2017) constructed a heterogeneous pulmonary (sub-)acinar model based on the algorithm proposed by Koshiyama and Wada (2015) and performed detailed and comprehensive simulations on the fate of aerosols in the acinar depths. Even though that isotropic motions are acknowledged to capture the macroscopic motion of lung expansion, the motion of acinar remains controversial (Hofemeier & Sznitman, 2016). In contrast to the isotropic assumption of acinar movement, the spatial expansion and contraction of the acinar walls were assumed to follow the anisotropic motion of the chest (De Groote et al., 1997; Plathow et al., 2004), which was smaller in the coronal (right-left) direction than that in the axial (head-foot) and sagittal (back-front, Z) directions with a ratio of 0.375:1:1 in some research (Li et al., 2023; Talaat & Xi, 2017; Xi et al., 2021). Moreover, Hofemeier and Sznitman (2016) explored in numerical simulations the influence of anisotropic acinar expansion on the deposition of inhaled aerosols and suggested that anisotropy modulates the deposition sites and fractions of particles in the size range of 0.5–0.75 μm.

However, the natural pulmonary acinar motion should be a complex passive deformation under pressure between the lung and the environment. The chest's outward elastic recoil and the lungs' inward elastic recoil lead to a change of transmural pressure, which drives the lungs to expand and contract passively. As a result, airflow and aerosol are inhaled and expelled out of the lungs. The mentioned hereinbefore, either the isotropic or anisotropic motion of the acinar wall predefined by the dynamic mesh approach fails to capture the passive deformation process of the acinar wall, not to mention the structure characteristics such as structural displacement and stress distribution. Using the fluid-solid Interaction (FSI) approach, the passive deformation of the lungs under transmural pressure can be obtained by applying varying pressure to the exterior of the alveolar model to mimic the real deformation of alveoli during respiration, shedding new light on accurate prediction of alveoli movements. Dailey and Ghadiali (2007) developed a two-dimensional FSI computational alveolar model and applied an oscillatory pressure to the tissue to generate airflow within the alveolus. Then they investigated how tissue mechanical properties and breathing patterns influence deep-lung flow fields and particle dynamics. Iranica et al. (2016) used a three-dimensional honeycomb-like FSI alveolar sac model proposed by Fung (1988) and studied the flow field and the mechanical behavior of alveolar wall tissue. Monjezi et al. (2017) studied aerosol deposition based on this FSI model (Iranica et al., 2016) and suggested that several breathing cycles are necessary for the accurate deposition of submicron particles. Chen et al. (2021; 2019) studied the effects of lung diseases (idiopathic interstitial pneumonias (2019) and pulmonary fibrosis (2021)) on the alveolar sac flow field and mechanics by using the FSI method and demonstrated that the lung diseases had a significant effect on airflow and lung function. However, the models in the above FSI studies were either limited to 2 dimensions or contained only alveolar sacs or simple bifurcating models. To date, FSI studies based on 3-dimensional multi-generation acinar models have yet to be reported. Furthermore, major of the aforementioned FSI studies focus on the flow field and structure mechanics, while the dynamics and deposition of aerosols

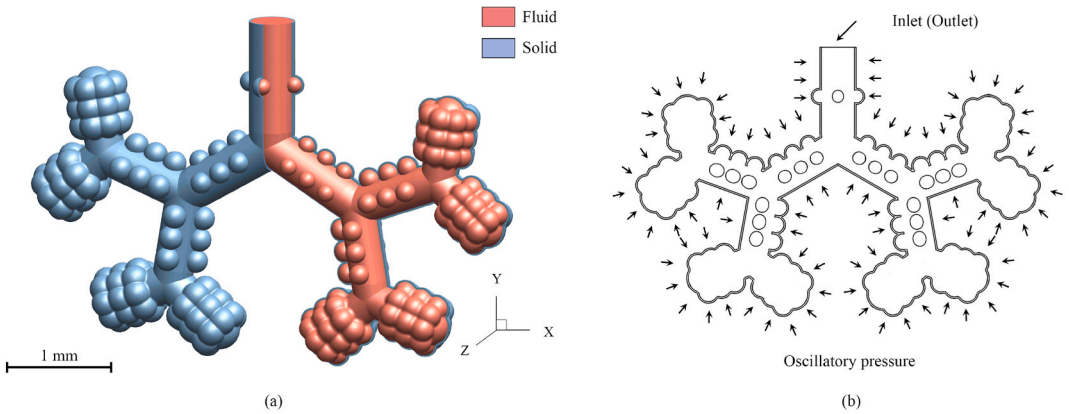

Fig. 1. Schematic of model and applied loads: (a) four-generation human pulmonary acinar model adopted from our previous work (Li et al., 2023); (b) applied loads outside the acinar model.

involving FSI are rare in the acinar depths.

In the current study, we present a computational analysis of the airflow, structural mechanics, and aerosol dynamics in the human pulmonary acinar region. For such purposes, we adopt a four-generation acinar model developed in our previous work (Li et al., 2023) and apply an oscillatory pressure on the outface of the model to generate structure deformation and airflow. With such tools at hand, we investigate the structural mechanics and airflow characteristics, as well as the transport and deposition of aerosol in the size range of 0.1–5 μm under cyclic breathing conditions.

2. Method

2.1. Acinar model and boundary conditions

In our previous work, a four-generation human pulmonary acinar model was developed to investigate the influence of wall motion and interparticle collisions on aerosol deposition (Li et al., 2023), which was established based on Weibel (1963) and shared well consistent with the literature on the ratio of ductal volume (Haefeli-Bleuer & Weibel, 1988; Ma & Darquenne, 2011). We adopted the acinar model as the fluid domain of the FSI model in the present work (Fig. 1(a)). The thickness of the solid domain was set as 25 μm according to research (Lai-Fook & Hyatt, 2000; Politi et al., 2010) to present healthy acinar wall similar to Chen et al. (2019). The acinar wall tissue was assumed to be a linearly elastic material (Dailey & Ghadiali, 2007; Iranica et al., 2016). Young's modulus of 8 kPa and Poisson's ratio of 0.42 was taken for the linear elastic model (Iranica et al., 2016).

At rest, lungs are elastic structures like balloons that tend to collapse. At the same time, the chest wall has elastic recoil tending to expand, and the inward elastic recoil of the lung exactly opposes the outward-acting elastic recoil of the chest wall (Marconi & De Lazzari, 2020; Silva & Gama de Abreu, 2018). The pressure difference between the alveolar pressure and the intrapleural pressure is the transmural pressure across the lung (i.e., TPP). During inspiration, the diaphragm and the inspiratory intercostal muscles actively contract, and the TPP increases by a value of 200 Pa, leading to the expansion of the lungs. Expansion of the lungs creates subatmospheric pressure in the alveoli, leading to airflow into the alveoli down the pressure gradient. During expiration, the diaphragm and inspiratory intercostal muscles cease contracting and relax, and TPP decreases to the value at rest, resulting in the passive recoil of the lungs to its original dimensions. Decreased lung dimensions lead to the alveolar pressure surpassing the atmospheric pressure; as a result, air flows from the alveoli to the atmosphere. In a nutshell, the change of TPP drives the deformation of the lung, which in turn drives the flow field. Therefore, we apply a sinusoidal oscillatory pressure to the external surface of the acinar model to generate airflow, as shown in Fig. 1(b). The pressure of inlet (outlet during expiration) is set to zero as the reference pressure (Chen et al., 2019; Dailey & Ghadiali, 2007; Iranica et al., 2016).

The magnitude of the applied pressure is considerably decreased by a coefficient of 0.2 to achieve a physiological volume expansion considering the effect of the tissue surrounding the alveolar sac, which is similar to Iranica et al. (2016). Hence, the oscillatory pressure load can be expressed as:

$$p_{load} = -\frac{p_0}{2} + \frac{p_0}{2}\cos\left(\frac{2\pi}{T}t\right) \tag{1}$$

where $p_0 = 40$ Pa is the change in applied pressure, $T = 4$ s is the respiratory period.

To verify if our FSI model produces physiological changes in model volume, we compared the volume change rate with the literature. Based on measurements by Haefeli-Bleuer and Weibel (1988), the functional residual capacity is about 3 L, and the tidal volume is about 600 mL, which would yield a 20% change in the lung volume. Our FSI model produced a 21% change in model volume. Therefore, our FSI model produced physiological changes in model volume consistent with reality.

2.2. Numerical simulations

Fluid flow in the pulmonary acinar region is assumed as isothermal and incompressible. The governing equations are the incompressible continuity and Navier-Stokes equations expressed as:

$$\rho_f \frac{\partial u_{f,i}}{\partial x_i} = 0 \tag{2}$$

$$\rho_f \left(\frac{\partial u_{f,i}}{\partial t} + \frac{\partial u_{f,i}u_{f,j}}{\partial x_j}\right) = -\frac{\partial p}{\partial x_i} + \frac{\sigma_{ij}^f}{\partial x_j} + f_{f,i} \tag{3}$$

$$\sigma_{ij}^f = -p\delta_{ij} + \mu\left(\frac{\partial u_{f,i}}{\partial x_j} + \frac{\partial u_{f,j}}{\partial x_i}\right) \tag{4}$$

where $u_{f,i}$ is the fluid velocity, ρ_f is the fluid density, p is the pressure, σ_{ij}^f is the fluid Cauchy stress tensor, $f_{f,i}$ is the fluid gravity, δ_{ij} is the Kronecker delta function and μ is the fluid viscosity.

The structure deformation of the solid domain is governed by momentum conservation equations expressed as:

$$\rho_s \frac{\partial^2 d_i^s}{\partial t^2} = \frac{\partial \sigma_{ij}^s}{\partial x_j} + f_{s,i} \tag{5}$$

$$\sigma_{ij}^s = C_{ijkl} \varepsilon_{kl} \tag{6}$$

where ρ_s is the solid density, d_i^s is the solid displacement, σ_{ij}^s is the solid Cauchy stress tensor, $f_{s,i}$ is the solid gravity, C_{ijkl} is the elasticity tensor, and ε_{kl} is the infinitesimal strain tensor. According to Hooke's law, C_{ijkl} and ε_{kl} can be expressed as:

$$C_{ijkl} = \frac{E}{2(1+\upsilon)}\left(\delta_{il}\delta_{jk} + \delta_{ik}\delta_{jl}\right) + \frac{E\upsilon}{(1+\upsilon)(1-2\upsilon)}\delta_{ij}\delta_{kl} \tag{7}$$

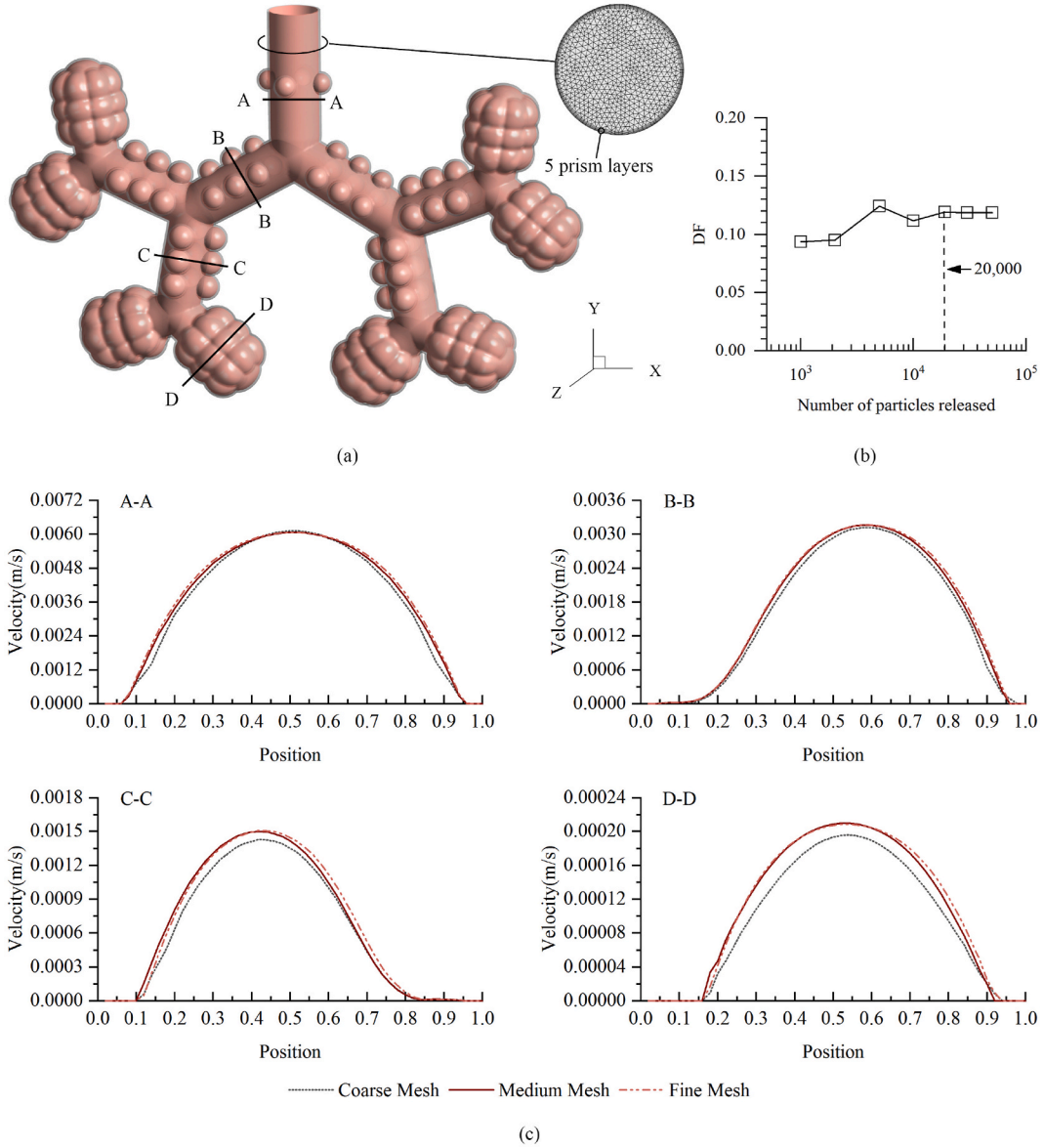

Fig. 2. Mesh-independent analyses and particle-count independent test. Mesh-independent analyses were conducted with coarse mesh, medium mesh, and fine mesh. The according number of elements in the fluid domain is 2.44 M , 3.79 M, and 5.02 M; Ones in the solid domain are 1.66 M, 2.47 M, and 3.38 M, respectively. Fifty points were selected equally spaced at four lines located in ABCD in the plane Z = 0 (a). The fluid velocities at those points at the peak inhalation (t = 1 s) were compared (c) to get mesh-independent results. (b): particle-count independent test was conducted by varying the number of released particles from 1,000 to 50,000.

$$\varepsilon_{kl} = \frac{1}{E}\left[\sigma^s_{kl} - \upsilon\left(\sigma^s_{ii}\delta_{kl} - \sigma^s_{kl}\right)\right] \tag{8}$$

where E is the Young's modulus, and υ is the Poisson ratio.

In the FSI model, the displacement, velocity and stress continuity are achieved by satisfying the flowing boundary conditions at the interface between the fluid and solid domains.

$$d^f_i = d^s_i \tag{9}$$

$$n_j\sigma^f_{ij} = n_j\sigma^s_{ij} \tag{10}$$

$$n_i u_{f,i} = n_i u_{s,i} \tag{11}$$

where d^f_i and d^s_i are the fluid and solid displacements, n_j and n_i are the interface normal vector, typically directed from the fluid domain towards the solid domain (Fagbemi, S, 2020), and $u_{f,i}$ and $u_{s,i}$ are the fluid and solid velocity.

Particles in the aerodynamic diameter range of 0.1–5 μm acknowledged with the ability to enter the acinar region (Heyder, 2004; Hinds, 1999) were considered in the present study. A Lagrangian particle tracking model was used to track their trajectory. These aerosols were assumed as spherical and had no interplay with each other and no effect on fluid. The three major forces acting on aerosols were aerodynamic drag F_D, gravitational sedimentation F_g, and Brownian diffusion F_B. The governing equations of aerosol are provided in more detail in Li et al. (2023).

The structural model in Ansys 2020 R2 Fluent provides the ability to perform a FSI simulation completely within a Fluent session, referred to as "intrinsic FSI". In an intrinsic FSI context, the flow applies forces on the interface boundary with the solid, which will deform; the resulting displacements of the solid domain will in turn lead to a deformation of the fluid domain. Both the fluid and structural calculations are performed by Fluent. Airflow, structure deformation and particle transport were numerically simulated for five respiratory cycles (20 s). At the beginning of inspiration (t = 0 s), particles (N = 20,000) were distributed uniformly at the inlet and carried into the model by the inhaled airflow. Particles hitting the wall were assumed to be deposited and those hitting the inlet (outlet) were assumed to be escaped. In reality, the particles will have velocities when reaching generation 17 as a result of inertia, and escaped particles could reenter the computational domain and deposit in the next inhalation. While due to the lack of the geometries of the upper airway, their released velocities were assumed as zero (Li et al., 2023; Ma & Darquenne, 2011). Escaped particles were assumed unable to return. Only particles that remained in suspension within the model at the end of expiration were tracked for additional breathing cycles. The deposition fraction (DF) was calculated by DF = N'/N in this study, where N' is the number of particles deposited and N=20,000 is the number of particles injected.

The tetrahedral mesh was used to discretize the fluid and solid domains in Ansys ICEM CFD, and 5 layers of prism elements were adopted near the wall to ensure accurate resolution of the boundary shown in Fig. 2(a). Mesh-independent analyses were conducted with three different sizes of mesh (i.e., coarse mesh, medium mesh and fine mesh). The number of elements in the fluid domain is 2.44 M, 3.79 M and 5.02 M; Ones in the solid domain are 1.66 M, 2.47 M and 3.38 M, respectively. Fifty points were selected equally spaced at four lines located in ABCD in the plane Z = 0, shown in Fig. 2(a). The fluid velocities at those points at the peak inhalation (t = 1 s) were compared (Fig. 2(c)). Results showed that increasing the number of elements above 3.79 M and 2.47 M in the fluid and solid domains showed less than 1% of the differences. Therefore, the final mesh size of 3.79 M and 2.47 M in fluid and solid domains was

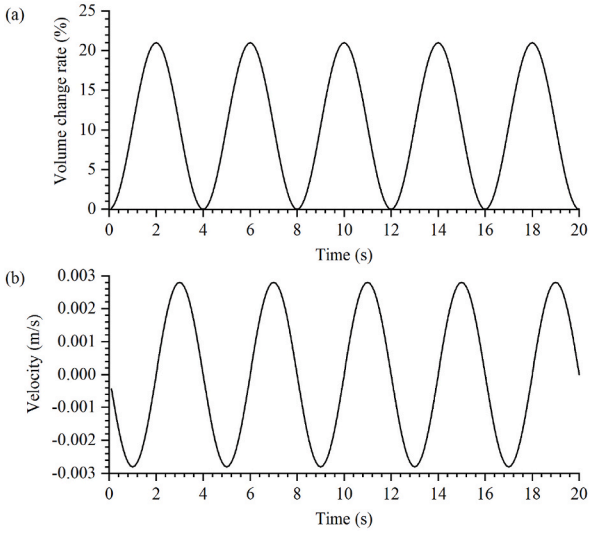

Fig. 3. Volume change rate (a) and resulting inlet velocity (b) of the acinar model under externally applied pressure over five respiratory cycles.

adopted. Then, 1 μm particles were used to achieve particle-count independent deposition simulations, and the number of released 1 μm particles was increased from 1,000 to 50,000 (Fig. 2(b)). It was discovered that the optimal particle amount for independence was 20,000 as the deposition variation was less than 0.5% when the number of released particles was above 20,000.

3. Result

3.1. Flow field

In the present study, we started with the flow field in the pulmonary acinar model under cyclic pressure using an FSI approach. Fig. 3 illustrates the rate of volume change and resulting inlet velocity of the model under externally applied pressure over five respiratory cycles. During the inhalation, the externally applied pressure decreased from the beginning of inspiration (t = 0 s) in the manner set in Eq. (1). As a result, the model kept expanding, and the airflow entered the model down the pressure gradient. At the end of inhalation (t = 2 s), the applied pressure and volume change rate reached their maximum value simultaneously, and the maximum volume change rate was 21%. Then the external pressure decreased during the exhalation, resulting in the exhalation of airflow and passive recoil of the model. At the end of exhalation (t = 4 s), the applied pressure and volume change rate decreased to zero simultaneously. The above process was one cycle, and so it was repeated for five cycles.

During inspiration (expiration), the airflow continuously entered (exited) the model, and the model inlet velocity increased and then decreased, reaching a peak velocity at the midpoint of inspiration (t = 1 s) and expiration (t = 3 s). To further characterize the flow field inside the alveoli, the flow streamlines at the peak inspiration (t = 1 s) were plotted in the symmetry plane (Z = 0), colored by the magnitude of flow field velocity (Fig. 4). Results showed that the velocity of the flow field was strongly influenced by the geometry of the model. At the same generation, the ductal flow field velocity exhibited a parabolic distribution at a much higher magnitude than that inside alveoli. Between the different generations, the ductal flow field velocity was maximum in generation 17, approximately 6 mm/s. As the generations increased, the velocity in the duct decreased obviously, until the velocity in the alveolar sac decreased below 0.5 mm/s, equivalent to the velocity in the alveoli. In terms of flow streamlines, the obvious recirculating flow was observed in the alveoli of generations 17–19. However, there was no recirculating flow in the sac, where the streamlines were radial.

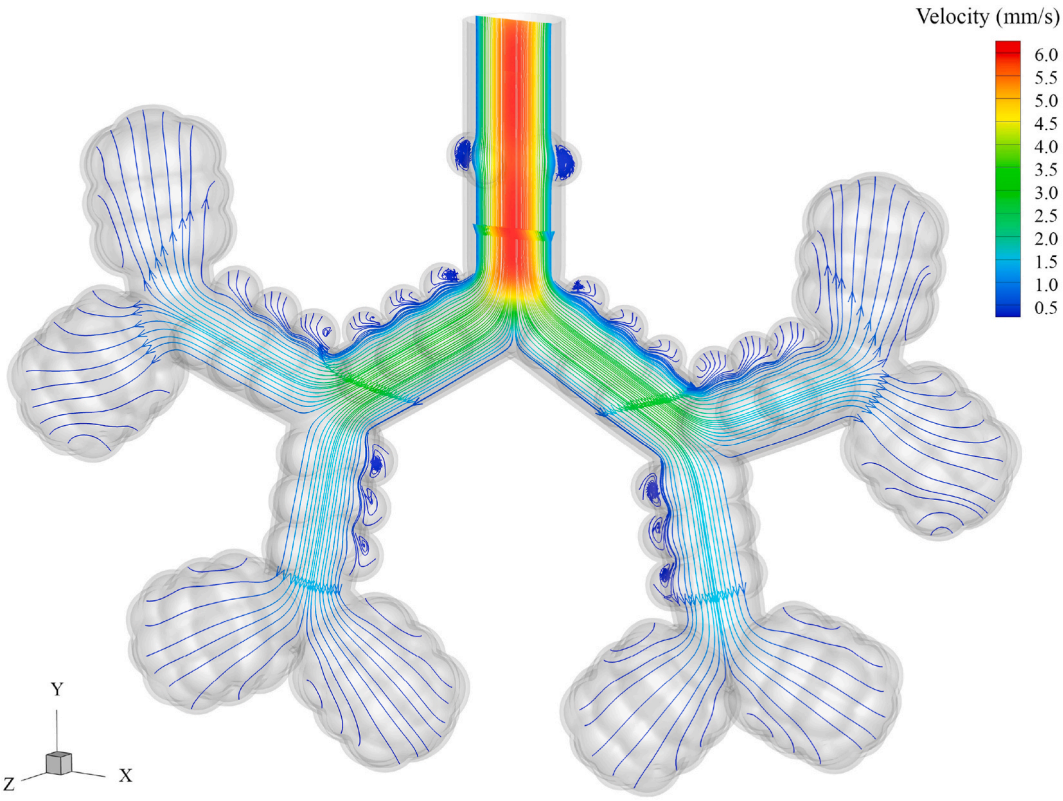

Fig. 4. Flow streamlines at the peak inspiration (t = 1 s) in the acinar model's symmetry plane (Z = 0), colored by the magnitude of flow field velocity.

3.2. Structural deformation and stress

During respiration, the acinar model expanded and contracted in accordance with the externally applied load and showed the changes in volume shown in Fig. 3(a). We selected four specific moments in a breathing period to further investigate the displacement of the tissue, as shown in Fig. 5. The tissue displacement reached a maximum of 200 μm at t = 2 s, locating at the end of the sac. At this moment, the acinar model was significantly deformed, with the sac region stretching longer in the axial direction, the end of the alveolar sac becoming smaller in diameter and bulging outwards, and the shape of the sac changing from the original cylindrical shape to ellipsoidal. The displacement decreased from the sac to generation 17, with a notable expansion of the alveoli in generation 19, a slight alveolar deformation in generation 18, and minimal deformation in generation 17. At 1 s and 3 s, the contours of the displacement of tissue were much similar due to the same volume change rate (Fig. 3(a)), the maximum displacement was 100 μm, and the maximum displacement point was also located at the end of the sac. The deformation of the acinar model was less pronounced at these two moments than at t = 2 s, but a slight stretch in the axial direction and a slight compression in the radial direction could be observed. At the end of the first breathing period, the tissue of the acinar model returned to its original shape with a maximum displacement of only 4 μm.

The structural stress was directly related to the tissue deformation; therefore, the stress contour was also remarkably similar due to the consistent volume change rate at 1 s and 3 s, as shown in Fig. 6, with a maximum stress of about 1.5 kPa. At t = 2 s, the tissue stress reached a maximum of approximately 2.5 kPa. When the first respiratory cycle was over, the model volume returned to its initial volume, with only a small amount of residual stress present in the ducts in generation 18, and the maximum stress was approximately 2.5 Pa.

It was noteworthy that the stress distribution on the acinar wall was significantly heterogeneous during breathing. Our results indicated that the stress distribution on the tissue was significantly influenced by the model geometry. Take the stress contour at t = 2 s (Fig. 6(b)), the stress on the alveoli was relatively few compared to the ducts in generation 17–19, and obvious concentrations of stress were found at the junction of the alveoli and the ducts compared to the area without alveolar coverage. Besides, the stress on the surface of the ducts increased with the generations and reached a maximum in the sac. The stress distribution at the alveolar-alveolar junction was higher than the other areas in the sac, making it a stress-concentration area.

3.3. Aerosol deposition

We next investigated how the number of breathing cycles correlated with aerosol deposition. The deposition fraction of each

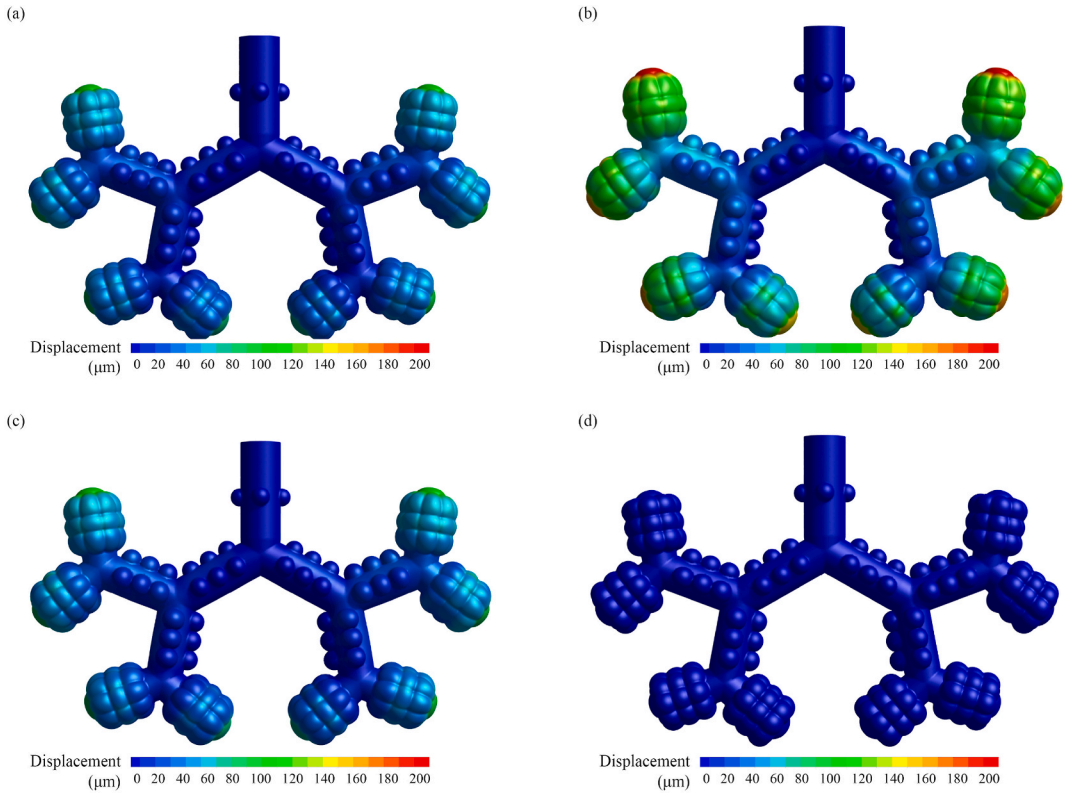

Fig. 5. Contour of tissue displacement at four specific moments in a breathing period; (a) t = 1 s, (b) t = 2 s, (c) t = 3 s, (d) t = 4 s.

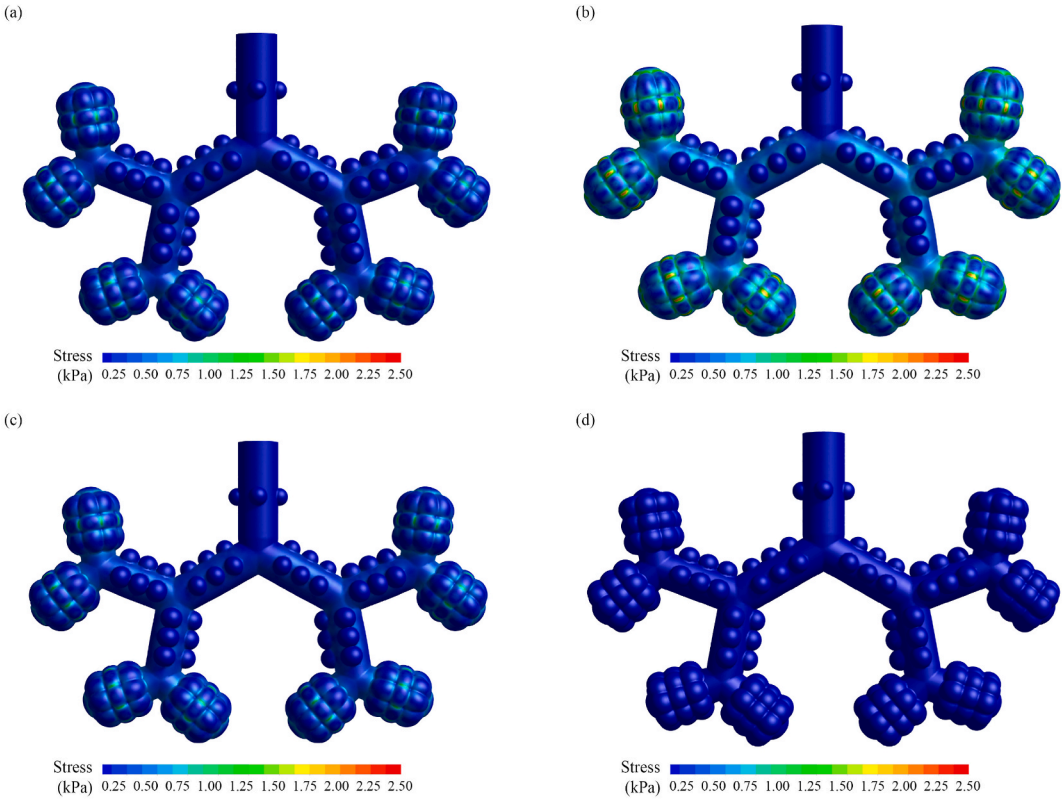

Fig. 6. Contour of tissue stress at four specific moments in a breathing period; (a) t = 1 s, (b) t = 2 s, (c) t = 3 s, (d) t = 4 s.

particle size after 1 respiratory cycle and 5 cycles were presented in Fig. 7.

The deposition fraction of 0.1 μm particles was 18.57% for 1 breathing cycle. The deposition rate decreased and then increased with particle size increasing, with the lowest deposition rate of 8.92% at 0.8 μm and the highest rate of 99.35% at 5 μm, showing a characteristic "U-shaped" trend. After 5 breathing cycles, the deposition fraction for all particle sizes increased significantly, especially for submicron particles. The deposition fraction of 0.1–1 μm particles increased by 1.78, 1.85, 1.84, 3.20, and 3.26 times compared to that after 1 cycle, respectively. Despite the significant influence of the number of cycles on the deposition fraction for each particle, the deposition fraction trend with particle size remained the "U-shaped" curve after 5 breathing cycles.

To further investigate the effect of the number of cycles on aerosol deposition, the deposition fraction of particles was calculated after each cycle (Fig. 8). 3 μm and 5 μm particle deposition rates reached a maximum (96.02% and 100%, respectively) in the second cycle, whereby the deposition rate of sub-micron particles increased linearly, with the deposition rate increasing by approximately the same amount after each cycle, reaching a maximum after 5 cycles.

Therefore, we mainly focused on the movement of aerosols in the first two cycles. Fig. 9 demonstrated the locations of 0.1 μm, 1 μm, and 3 μm particles in suspension at 2 s, 4 s, 6 s, and 8 s in the acinar model. To better describe the locations of particle suspension and deposition, the model was further divided into seven regions according to the location: D17, A17, D18, A18, D19, A19, and SAC, where D represents the ducts, and A represents the alveoli, as shown in Fig. 10. As an example, A18 refers to the alveoli in generation 18, and D19 to the ducts in generation 19.

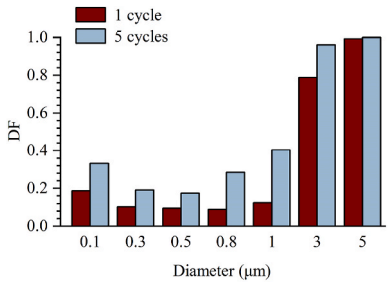

Fig. 7. Deposition fraction (DF) of each particle size after 1 respiratory cycle and 5 cycles.

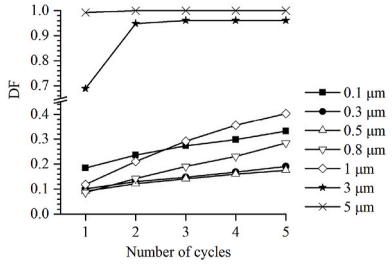

Fig. 8. Deposition fraction (DF) of particles after each cycle.

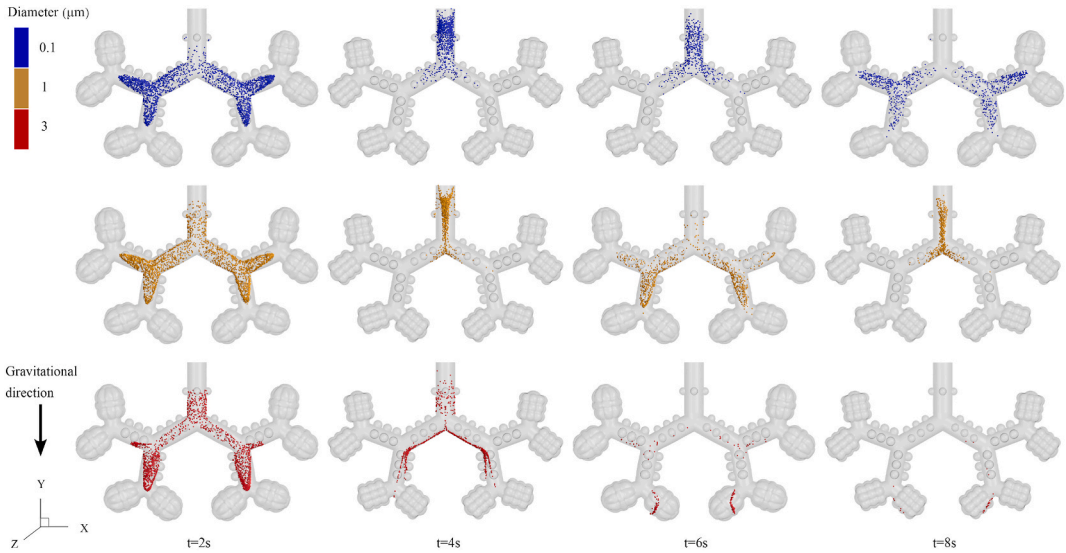

Fig. 9. Locations of 0.1 μm, 1 μm and 3 μm particles in suspension at 2 s, 4 s, 6 s, and 8 s in the acinar model.

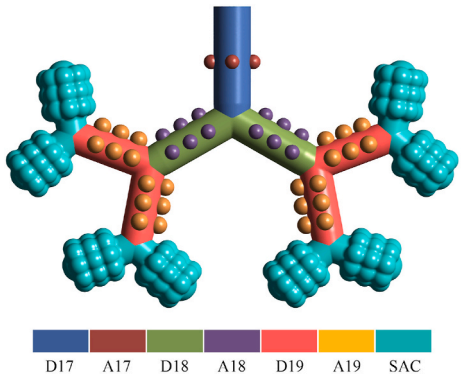

Fig. 10. Sketch of divided regions.

At 2 s, the first inspiratory phase was over, and the inhaled particles entered the alveolar model driven by the inspiratory airflow and reached the most distant distance. 0.1 μm particles deposited at the inlet ring (i.e., D17) within short time scales due to Brown motion (Hofemeier et al., 2017; Hofemeier & Sznitman, 2015), and the number of suspended 0.1 μm particles in generation 17 was minor. In contrast, 3 μm particles were suspended further down than 0.1 μm and 1 μm particles and had partly deposited in D18 as an outcome of gravity, resulting in a lower density of particles suspended in generation 18.

At 4 s, the first expiratory period was completed, and particles were carried to the outlet (some particles escaped from the outlet) by the exhaust airflow. The majority of 0.1 μm particles moved to generation 17 and suspended there uniformly in space, with a small portion at the upper part of generation 18. In contrast, 1 μm particles were concentrated in the central part of the duct of generation 17.

During the exhalation phase, the exhaust airflow induced by the contraction of the model rushed towards the outlet and converged at the bifurcations. As a result, 1 μm particles merged in the central part of the model, forming a high-density area. This phenomenon demonstrated the influence of convection on the dynamics of 1 μm particles. Only a minor of 3 μm particles moved to generation 17. Most of them continued to move downwards in the direction of gravity and formed a high-density zone in the lower side of generation 18.

Fig. 11 illustrates the deposition fraction of particles in size range of 0.1–5 μm in the divided regions after the first, second, and fifth respiratory cycles.

During the second respiratory cycle, particles still suspended in the model re-entered the model with the inspiratory airflow. At the beginning of the second cycle (t = 4 s), suspended particles were located deeper into the model than at the beginning of the first cycle (t = 0 s), so that 0.1 μm and 1 μm particles at 6 s were suspended further away than at 2 s and mainly deposited in generation 18 (Fig. 11), especially for 1 μm particles. As the number of cycles increased, submicron particles penetrated more deeply into the model, and after five respiratory cycles, a small amount was even deposited in generation 19 (Fig. 11). Most of the 3 μm particles were deposited after the first respiratory cycle, with the remaining small amount of suspended particles continuing to move and deposit in the direction of gravity; hence the deposition fraction of 3 μm particles slightly increased in the second cycle.

At the end of the second respiration (8 s), the suspended 0.1 μm and 1 μm particles moved upwards with the airflow to generations 17 and 18, similar to the distribution at the end of the first breathing cycle. The difference was that the density of the particles decreased due to the ongoing deposition. In addition, the location of suspended 0.1 μm and 1 μm aerosol shifted downwards again compared to that at 4 s after another respiration cycle, and this shift would gradually increase in subsequent respiration cycles and contribute to the deeper dispersion of submicron particles into the model.

The effect of cycles on the deposition and transport of submicron particles was significant. As the respiration cycle increases, 0.1–0.5 μm particles continued to be deposited in D17 and D18 with deeper dispersion distances as an outcome of Brownian motion. It should be noted that as the particle size increased, the dominant effect of Brownian forces diminished; hence the deposition fraction of 0.1–0.5 μm particles decreased with the diameter increasing. 0.8 μm and 1 μm particles were only partially deposited in D17 during the first cycle, with deposition occurring largely in D18 during the subsequent cycles. However, multi-respiratory cycles played a minor role in the deposition of 3 μm and 5 μm, whereby gravity dominated principally their transport and deposition.

4. Discussion

Accurate lung movements are essential to obtain the flow field and aerosol motion characteristics in the acinar region. In contrast to research which used predefined wall motion, we developed a four-generation FSI model and applied an oscillatory pressure on the outface of the model to generate structure deformation and airflow. The airflow characteristics and structural mechanics, as well as the transport and deposition of aerosol in the size range of 0.1–5 μm were simulated for five breathing cycles.

Our results demonstrated the absence of recirculating flow in the sac, where the streamlines were radial, in agreement with the literature (Sznitman, 2013; Talaat & Xi, 2017). Research show that the alveolar flow pattern is determined by the ratio of alveolar/ductal flow (Tsuda et al., 1995) and that recirculation flow is absent when the ratio of alveolar/ductal flow ratio >0.02 (Ma & Darquenne, 2011; Sznitman et al., 2007). In the present study, the flow rate and velocities in ducts decreased with the continuous branching of the acinar model until the velocity in the alveolar sac was equivalent to the velocity in the alveoli. As a result, the alveolar/duct flow ratio exceeded 0.02 and the recirculation flow was absent in the sac.

The use of the FSI approach was not only helpful in obtaining an accurate prediction of alveoli passive deformation but also contributed to the capture of the structural mechanics, which cannot be achieved by predefined velocities or wall motion using dynamic grid method. In contrast to the published FSI research limited to 2 dimensions or containing only alveolar sacs or simple bifurcating models, we developed a four-generation FSI model, which is to the best of our knowledge the most comprehensive FSI model, and investigated the structural deformation and stress. Our results showed that the deformation of the acinar wall mainly occurs in the sac. In contrast, the deformation of ducts was considerably less compared to the sac (Fig. 5). Forrest (1970) showed that the change of lung volume during breathing was mainly realized by the deformation of alveoli and the sac, while the deformation of bronchi and pulmonary ducts was quite small. This conclusion is consistent with our results.

We next investigated the movement of particles in the size range of 0.1–5 μm within five respiration cycles and recaptured the “U-shaped” curve of aerosol deposition with the diameter (Hofemeier et al., 2017; Sznitman, 2022). Our research reconfirmed the dominant role of Brownian force and gravity on small particles and large particles, respectively, from the perspectives of total deposition fraction (Fig. 7), suspended aerosol position at typical moments (Fig. 9) and regional deposition fraction (Fig. 11). Our study suggested that multiple respiratory cycles were essential for adequate deposition or escape of submicron particles, especially those with particle sizes around 1 μm, contributing to the higher deposition fraction and deeper dispersion of submicron particles in the acinar depth. However, multiple respiratory cycles had a negligible influence on the deposition of large particles, which were dominated by gravity.

To validate the deposition data of aerosol in this study, the aerosol deposition fraction after 1 respiratory cycle was compared with similar studies which used similar tubular bifurcating models with hemispheres (Kolanjiyil & Kleinstreuer, 2019; Ma & Darquenne, 2011) and Hinds (1999), as shown in Fig. 12. Our results remained in good agreement with these research.

The major limitation of our study lies in the considerable gap between the real human acinus and our simplified model. In reality, enormous alveoli (Matthias et al., 2004) are arranged in clusters throughout the lungs and share parenchymal walls with neighbors. Due to the enormous number of alveoli (Matthias et al., 2004) and highly complicated acinar morphometries, there is a rather large gulf in getting a realistic computational or in vitro acinar model. Despite the development of micro X-ray computed tomography,

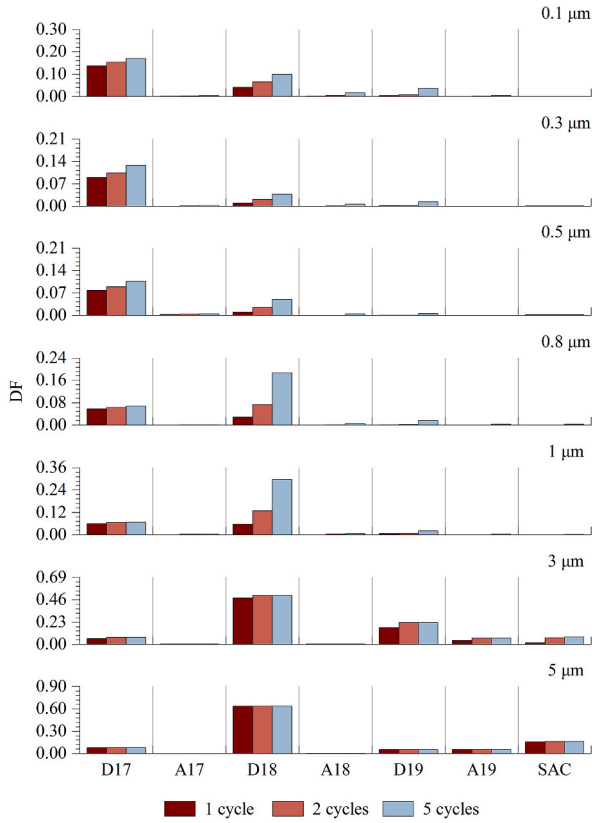

Fig. 11. Regional deposition fraction (DF) of particles in size range of 0.1–5 μm after the first, second and fifth respiratory cycles.

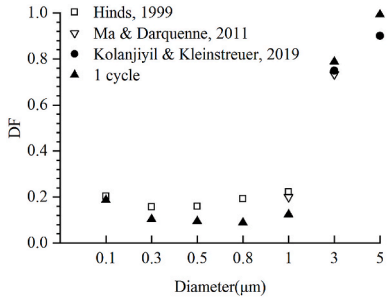

Fig. 12. Comparison of the deposition fraction (DF) in the present study with similar research (Ma & Darquenne, 2011; Kolanjiyil & Kleinstreuer, 2019) and Hinds (1999).

making it available to reconstruct small rodent acinar models (Sera et al., 2017; Sznitman et al., 2010; Tsuda et al., 2008), there is still a considerable gap in getting a realistic human acinar model due to the highly complicated acinar morphometries and imaging resolution limitations. The model used in this study has been simplified and falls considerably short of what actually happens in human lungs. Therefore, our results are limited, epically for the structural results which are strongly related to the geometry of the model (Sarabia-Vallejos et al., 2019; Yilmaz et al., 2020). In further research, we would apply the FSI approach to a more anatomically realistic model (e.g., the space-filling model of Koshiyama and Wada (2015)) to get more realistic results.

There are several other limitations in the present study: i) the acinar wall tissue was assumed to be a linearly elastic material in our FSI model. However, the realistic acinar wall should be a nonlinearly and comprehensive material. In the future, the non-linear acinar wall material could be included in our FSI model. ii) FSI analysis requires high-quality meshes and is prone to negative meshes at high levels of deformation, making it more challenging to simulate the structural mechanism of the multi-generation acinar model under high tidal volume breathing conditions.

5. Conclusion

In summary, we developed a four-generation FSI model and performed a computational analysis which addressed both airflow, structural mechanics and aerosol dynamics in the acinar depth. With such tools at hand, we revisited the absence of the recirculating flow in the sac. Our structural results showed that the deformation of the acinar wall mainly occurred in the sac, with a maximum displacement of 200 μm. The stress distribution on the acinar wall was found significantly heterogeneous. Obvious concentrations of stress were found at the junction of the alveoli and the ducts or the junction of the alveoli and alveoli in the sac. We next investigated the effect of breathing cycles and aerosol diameter on aerosol transport and deposition within five respiration cycles. Our results highlighted how respiratory cycles yielded higher deposition fraction and deeper dispersion for submicron particles, which had a negligible influence on the deposition of large particles.

Declaration of competing interest

The authors declare that they have no known competing financial interests or personal relationships that could have appeared to influence the work reported in this paper.

Data availability

Data will be made available on request.

References

Amirav, I., & Newhouse, M. T. (2012). Deposition of small particles in the developing lung. *Paediatric Respiratory Reviews, 13*(2), 73–78. https://doi.org/10.1016/j.prrv.2011.05.006

Ardila, R., Horie, T., & Hildebrandt, J. (1974). Macroscopic isotropy of lung expansion. *Respiration Physiology, 20*(2), 105–115. https://doi.org/10.1016/0034-5687(74)90100-5

Ari, A., & Fink, J. B. (2013). Aerosol therapy in children: Challenges and solutions. *Expert Review of Respiratory Medicine, 7*(6), 665–672. https://doi.org/10.1586/17476348.2013.847369

Chen, L., Tao, W., Ji, W., Lu, Y., & Zhao, X. (2021). Effects of pulmonary fibrosis and surface tension on alveolar sac mechanics in diffuse alveolar damage. *Journal of Biomechanical Engineering, 143*(8). https://doi.org/10.1115/1.4050789

Chen, L., Zhao, X., & Sznitman, J. (2019). Characterization of air flow and lung function in the pulmonary acinus by fluid-structure interaction in idiopathic interstitial pneumonias. *PLoS One, 14*(3), Article e0214441. https://doi.org/10.1371/journal.pone.0214441

Dailey, H. L., & Ghadiali, S. N. (2007). Fluid-structure analysis of microparticle transport in deformable pulmonary alveoli. *Journal of Aerosol Science, 38*(3), 269–288. https://doi.org/10.1016/j.jaerosci.2007.01.001

De Groote, A., Wantier, M., Cheron, G., Estenne, M., & Paiva, M. (1997). Chest wall motion during tidal breathing. *Journal of Applied Physiology, 83*(5), 1531–1537. https://doi.org/10.1152/jappl.1997.83.5.1531, 1985.

Fagbemi, S. (2020). *Multiscale fluid-solid interaction in deformable porous media*. University of Wyoming.

Forrest, J. B. (1970). The effect of changes in lung volume on the size and shape of alveoli. *Journal of Physiology, 210*(3), 533–547. https://doi.org/10.1113/jphysiol.1970.sp009225

Fung, Y. C. (1988). A model of the lung structure and its validation. *Journal of Applied Physiology, 64*(5), 2132–2141. https://doi.org/10.1152/jappl.1988.64.5.2132

Gil, J., Bachofen, H., Gehr, P., & Weibel, E. R. (1979). Alveolar volume-surface area relation in air- and saline-filled lungs fixed by vascular perfusion. *Journal of Applied Physiology: Respiratory, Environmental & Exercise Physiology, 47*(5), 990–1001. https://doi.org/10.1152/jappl.1979.47.5.990

Gil, J., & Weibel, E. R. (1972). Morphological study of pressure-volume hysteresis in rat lungs fixed by vascular perfusion. *Respiration Physiology, 15*(2), 190–213. https://doi.org/10.1016/0034-5687(72)90098-9

Haefeli-Bleuer, B., & Weibel, E. R. (1988). Morphometry of the human pulmonary acinus. *The Anatomical Record, 220*(4), 401–414. https://doi.org/10.1002/ar.1092200410

Heyder, J. (2004). Deposition of inhaled particles in the human respiratory tract and consequences for regional targeting in respiratory drug delivery. *Proceedings of the American Thoracic Society, 1*(4), 315–320. https://doi.org/10.1513/pats.200409-046TA

Hinds, W. C. (1999). *Aerosol technology, properties, behaviour, and measurement of airborne particles*. John Wiley & Sons Inc.

Hofemeier, P., Koshiyama, K., Wada, S., & Sznitman, J. (2017). One (sub-)acinus for all: Fate of inhaled aerosols in heterogeneous pulmonary acinar structures. *European Journal of Pharmaceutical Sciences, 113*, 53–63. https://doi.org/10.1016/j.ejps.2017.09.033

Hofemeier, P., & Sznitman, J. (2015). Revisiting pulmonary acinar particle transport: Convection, sedimentation, diffusion, and their interplay. *Journal of Applied Physiology, 118*(11), 1375–1385. https://doi.org/10.1152/japplphysiol.01117.2014

Hofemeier, P., & Sznitman, J. (2016). The role of anisotropic expansion for pulmonary acinar aerosol deposition. *Journal of Biomechanics, 49*(14), 3543–3548. https://doi.org/10.1016/j.jbiomech.2016.08.025

Iranica, S., Monjezi, M., & Saidi, M. S. (2016). Fluid-structure interaction analysis of airrow in pulmonary alveoli during normal breathing in healthy humans. *Scientia Iranica, 23*(4), 1826–1836. https://doi.org/10.24200/sci.2016.3929

Kato, T., Yashiro, T., Murata, Y., Herbert, D. C., Oshikawa, K., Bando, M., Ohno, S., & Sugiyama, Y. (2003). Evidence that exogenous substances can be phagocytized by alveolar epithelial cells and transported into blood capillaries. *Cell and Tissue Research, 311*(1), 47–51. https://doi.org/10.1007/s00441-002-0647-3

Kolanjiyil, A. V., & Kleinstreuer, C. (2019). Modeling Airflow and Particle Deposition in a Human Acinar Region. *Computational and Mathematical Methods in Medicine, 2019*, 5952941. https://doi.org/10.1155/2019/5952941.

Koshiyama, K., & Wada, S. (2015). Mathematical model of a heterogeneous pulmonary acinus structure. *Computers in Biology and Medicine, 62*, 25–32. https://doi.org/10.1016/j.compbiomed.2015.03.032

Lai-Fook, S. J., & Hyatt, R. E. (2000). Effects of age on elastic moduli of human lungs. *Journal of Applied Physiology, 89*(1), 163–168. https://doi.org/10.1152/jappl.2000.89.1.163

Leung, N. H. L. (2021). Transmissibility and transmission of respiratory viruses. *Nature Reviews Microbiology, 19*(8), 528–545. https://doi.org/10.1038/s41579-021-00535-6

Li, P., Guo, W., Fan, J., Su, C., Zhao, X., & Xu, X. (2023). Aerosol deposition in the pulmonary acinar region: Influence of wall motion and interparticle collisions. *Journal of Aerosol Science, 167*, Article 106077. https://doi.org/10.1016/j.jaerosci.2022.106077

Ma, B., & Darquenne, C. (2011). Aerosol deposition characteristics in distal acinar airways under cyclic breathing conditions. *Journal of Applied Physiology, 110*(5), 1271–1282. https://doi.org/10.1152/japplphysiol.00735.2010

Ma, B., & Darquenne, C. (2012). Aerosol bolus dispersion in acinar airways–influence of gravity and airway asymmetry. *Journal of Applied Physiology, 113*(3), 442–450. https://doi.org/10.1152/japplphysiol.01549.2011

Marconi, S., & De Lazzari, C. (2020). In silico study of airway/lung mechanics in normal human breathing. *Mathematics and Computers in Simulation, 177*, 603–624. https://doi.org/10.1016/j.matcom.2020.05.014

Matthias, O., Nyengaard, J. R., Anja, J., Lars, K., Marion, V., Thorsten, W., Joachim, R., & Gundersen, H. J. R. G. (2004). The number of alveoli in the human lung. *American Journal of Respiratory and Critical Care Medicine, 169*(1), 120–124. https://doi.org/10.1164/rccm.200308-1107OC

Monjezi, M., Saidi, M. S., & Ahmadi, G. (2017). Submicron particle deposition in pulmonary alveoli during cyclic breathing. *Scientia Iranica, 24*, 1975–1984. https://doi.org/10.24200/SCI.2017.4292

Nemmar, A., Hoet, P. H., Vanquickenborne, B., Dinsdale, D., Thomeer, M., Hoylaerts, M. F., Vanbilloen, H., Mortelmans, L., & Nemery, B. (2002). Passage of inhaled particles into the blood circulation in humans. *Circulation, 105*(4), 411–414. https://doi.org/10.1161/hc0402.104118

Plathow, C., Ley, S., Fink, C., Puderbach, M., Heilmann, M., Zuna, I., & Kauczor, H. U. (2004). Evaluation of chest motion and volumetry during the breathing cycle by dynamic MRI in healthy subjects: Comparison with pulmonary function tests. *Investigative Radiology, 39*(4), 202–209. https://doi.org/10.1097/01.rli.0000113795.93565.c3

Politi, A. Z., Donovan, G. M., Tawhai, M. H., Sanderson, M. J., Lauzon, A.-M., Bates, J. H. T., & Sneyd, J. (2010). A multiscale, spatially distributed model of asthmatic airway hyper-responsiveness. *Journal of Theoretical Biology, 266*(4), 614–624. https://doi.org/10.1016/j.jtbi.2010.07.032

Sarabia-Vallejos, M. A., Zuñiga, M., & Hurtado, D. E. (2019). The role of three-dimensionality and alveolar pressure in the distribution and amplification of alveolar stresses. *Scientific Reports, 9*(1), 8783. https://doi.org/10.1038/s41598-019-45343-4

Sera, T., Higashi, R., Naito, H., Matsumoto, T., & Tanaka, M. (2017). Distribution of nanoparticle depositions after a single breathing in a murine pulmonary acinus model. *International Journal of Heat and Mass Transfer, 108*, 730–739.

Silva, P. L., & Gama de Abreu, M. (2018). Regional distribution of transpulmonary pressure. *Annals of Translational Medicine, 6*(19), 385. https://doi.org/10.21037/atm.2018.10.03

Singh, D., Agusti, A., Anzueto, A., Barnes, P. J., Bourbeau, J., Celli, B. R., Criner, G. J., Frith, P., Halpin, D. M. G., Han, M., Varela, M. V. L., Martinez, F., Oca, M. M.d., Papi, A., Pavord, I. D., Roche, N., Sin, D. D., Stockley, R., Vestbo, J., Wedzicha, J. A., & Vogelmeier, C. (2019). Global strategy for the diagnosis, management, and prevention of chronic obstructive lung disease: The GOLD science committee report 2019. *European Respiratory Journal, 53*(5), Article 1900164. https://doi.org/10.1183/13993003.00164-2019

Sundh, J., Ställberg, B., Lisspers, K., Kämpe, M., & Montgomery, S. (2015). Comparison of the COPD assessment test (CAT) and the clinical COPD questionnaire (CCQ) in a clinical population. *COPD: Journal of Chronic Obstructive Pulmonary Disease, 13*(1), 57–65. https://doi.org/10.3109/15412555.2015.1043426

Sung, J. C., Pulliam, B. L., & Edwards, D. A. (2007). Nanoparticles for drug delivery to the lungs. *Trends in Biotechnology, 25*(12), 563–570. https://doi.org/10.1016/j.tibtech.2007.09.005

Sznitman, J. (2013). Respiratory microflows in the pulmonary acinus. *Journal of Biomechanics, 46*(2), 284–298. https://doi.org/10.1016/j.jbiomech.2012.10.028

Sznitman, J. (2022). Revisiting airflow and aerosol transport phenomena in the deep lungs with microfluidics. *Chemical Reviews, 122*(7), 7182–7204. https://doi.org/10.1021/acs.chemrev.1c00621

Sznitman, J., Heimsch, F., Heimsch, T., Rusch, D., & Rösgen, T. (2007). Three-dimensional convective alveolar flow induced by rhythmic breathing motion of the pulmonary acinus. *Journal of Biomechanical Engineering, 129*(5), 658–665. https://doi.org/10.1115/1.2768109

Sznitman, J., Sutter, R., Altorfer, D., Stampanoni, M., Roesgen, T., & Schittny, J. C. (2010). Visualization of respiratory flows from 3D reconstructed alveolar airspaces using X-ray tomographic microscopy. *Journal of Visualization, 13*(4), 337–345. https://doi.org/10.1007/s12650-010-0043-0

Talaat, K., & Xi, J. (2017). Computational modeling of aerosol transport, dispersion, and deposition in rhythmically expanding and contracting terminal alveoli. *Journal of Aerosol Science, 112*, 19–33. https://doi.org/10.1016/j.jaerosci.2017.07.004

Tsuda, A., Filipovic, N., Haberthür, D., Dickie, R., & Schittny, J. C. (2008). Finite element 3D reconstruction of the pulmonary acinus imaged by synchrotron X-ray tomography. *Journal of Applied Physiology, 105*(3), 964–976. https://doi.org/10.1152/japplphysiol.90546.2008

Tsuda, A., Henry, F. S., & Butler, J. P. (1995). Chaotic mixing of alveolated duct flow in rhythmically expanding pulmonary acinus. *Journal of Applied Physiology, 79*(3), 1055–1063. https://doi.org/10.1152/jappl.1995.79.3.1055

Weibel, E. R. (1963). *Morphometry of the human lung*. Berlin: Springer-Verlag.

Wu, S., Huang, J., Zhang, Z., Wu, J., Zhang, J., Hu, H., Zhu, T., Zhang, J., Luo, L., Fan, P., Wang, B., Chen, C., Chen, Y., Song, X., Wang, Y., Si, W., Sun, T., Wang, X., Hou, L., & Chen, W. (2021). Safety, tolerability, and immunogenicity of an aerosolised adenovirus type-5 vector-based COVID-19 vaccine (Ad5-nCoV) in adults: Preliminary report of an open-label and randomised phase 1 clinical trial. *The Lancet Infectious Diseases, 21*(12), 1654–1664. https://doi.org/10.1016/s1473-3099(21)00396-0

Xi, J., Talaat, M., Si, X. A., & Kitaoka, H. (2021). Micrometer aerosol deposition in normal and emphysematous subacinar models. *Respiratory Physiology & Neurobiology, 283*, Article 103556. https://doi.org/10.1016/j.resp.2020.103556

Yilmaz, C., Dane, D., Tustison, N., Song, G., Gee, J., & Hsia, C. (2020). In vivo imaging of canine lung deformation: Effects of posture, pneumonectomy, and inhaled erythropoietin. *Journal of Applied Physiology, 128*. https://doi.org/10.1152/japplphysiol.00647.2019